AJNR

Dual-Energy CT in the Evaluation of Intracerebral Hemorrhage of Unknown Origin: Differentiation between Tumor Bleeding and Pure Hemorrhage

S.J. Kim, H.K. Lim, H.Y. Lee, C.G. Choi, D.H. Lee, D.C. Suh, S.M. Kim, J.K. Kim and B. Krauss

AJNR Am J Neuroradiol 2012, 33 (5) 865-872
doi: https://doi.org/10.3174/ajnr.A2890
http://www.ajnr.org/content/33/5/865

ORIGINAL RESEARCH

Dual-Energy CT in the Evaluation of Intracerebral Hemorrhage of Unknown Origin: Differentiation between Tumor Bleeding and Pure Hemorrhage

S.J. Kim
H.K. Lim
H.Y. Lee
C.G. Choi
D.H. Lee
D.C. Suh
S.M. Kim
J.K. Kim
B. Krauss

BACKGROUND AND PURPOSE: Detection of underlying tumor in patients with unknown-origin acute ICH may be difficult because acute hematoma may mask enhancement of tumor on postcontrast CT. We intended to investigate the clinical utility of DECT in differentiating tumor bleeding from pure ICH.

MATERIALS AND METHODS: Using a dual-source CT scanner, we obtained TNC single-energy and postcontrast DECT scans for 56 patients with unknown-origin spontaneous ICH. From the 2 sets of postcontrast DECT images obtained with different tube energy, EA (equivalent to conventional postcontrast CT), VNC, color-coded iodine overlay, fusion images of iodine overlay and VNC images were produced. The diagnostic performances of fusion, EA, and combined EA and TNC images for detecting underlying tumors were compared.

RESULTS: Of the 56 patients, 17 had primary or metastatic tumors (18 lesions) and 39 had nontumorous ICH. The sensitivities of fusion, EA, and combined EA and TNC images for detecting brain tumors were 94.4%, 61.1%, and 66.7%, respectively, and their specificities were 97.4%, 92.3%, and 89.7%, respectively. The areas under the ROC curves were 0.964, 0.786, and 0.842, respectively. Overall, the diagnostic performance of fusion images was significantly superior to EA ($P = .006$) and combined EA and TNC ($P = .011$) images.

CONCLUSIONS: DECT may be useful in detecting underlying tumors in patients with unknown-origin ICH.

ABBREVIATIONS: AUC = area under curve; AVM = arteriovenous malformation; CNR = contrast-to-noise ratio; DECT = dual-energy CT; EA = enhanced average; HU = Hounsfield unit; ICH = intracerebral hemorrhage; MPR = multiplanar reformation; ROC = receiver operating characteristic analysis; SD = standard deviation; TNC = true noncontrast; VNC = virtual noncontrast

The global incidence of ICH ranges from 10 to 20 cases per 100,000 population.[1-3] Identification of underlying causes in spontaneous ICH is critical for the proper patient management. Although 78%–88% of spontaneous ICHs are caused by chronic hypertension or amyloid angiopathy, other causes may include underlying vascular abnormality, tumors, or impaired coagulation.[3] Noncontrast CT is the technique of choice for screening ICH, whereas contrast-enhanced CT or MR imaging may be necessary for assessing underlying causes.[4-6] CT angiography has become an important imaging tool for assessing the vascular origin in any patient without definite cause, though conventional angiography remains the reference standard for diagnosing underlying vascular lesions.[7-11]

Approximately 10% of all spontaneous ICHs are due to hemorrhages from brain tumors[4,12]; because most of these tumors have a solid enhancing portion, enhanced CT can be used for tumor identification.[5,13,14] However, acute ICH has a high attenuation on CT, which may mask contrast enhancement.[15] Although MR imaging may be more useful in detecting underlying tumors in patients with tumor bleeding,[5,13,16] acute ICH may show variable high signals on T1-weighted images, making it difficult to differentiate enhancement from high-signal-intensity hematoma.[13,16,17]

DECT can differentiate bone and iodine and hematoma and iodine.[18,19] Therefore, with DECT, the enhancing portion of a tumor can be differentiated more easily from an underlying hematoma. We investigated the clinical utility of DECT in the differentiation of tumor bleeding from pure ICH.

Materials and Methods

This prospectively designed study was approved by our institutional review board, and informed consent was obtained from all patients or family members.

Patients

The study cohort consisted of 56 patients (35 men, 21 women) with acute ICH. Patients were recruited between May 2008 and June 2010, and the mean patient age was 56 years (range, 19–92 years). All patients presented with no definite underlying cause of ICH. Patients with a clear history of trauma or obvious hypertensive ICH both clinically and on CT at the time of presentation were excluded because enhanced study is not generally indicated in those patients. Patients with definitive metastasis on initial imaging were also excluded. The

Received April 21, 2011; accepted after revision August 20.

From the Department of Radiology and Research Institute of Radiology (S.J.K., H.K.L., H.Y.L., C.G.C., D.H.L., D.C.S.), University of Ulsan College of Medicine, Asan Medical Center, Seoul, Korea; Department of Radiology (S.M.K.), East-West Neomedical Center, Kyung Hee University, College of Medicine, Seoul, Korea; Department of Radiology (J.K.K.), Chung-Ang University College of Medicine, Seoul, Korea; and Imaging and Therapy Division (B.K.), Siemens AG Healthcare Sector, Forchheim, Germany.

Paper previously presented in part at: 48th Annual Meeting of the American Society of Neuroradiology and the Neuroradiology Education and Research Foundation, May 15–20, 2010; Boston, Massachusetts.

Please address correspondence to Sang Joon Kim, MD, Department of Radiology and Research Institute of Radiology, University of Ulsan College of Medicine, Asan Medical Center, 86 Asanbyeongwon-Gil, Songpa-Gu, Seoul 138-736, Korea; e-mail: sjkimjb@amc.seoul.kr

http://dx.doi.org/10.3174/ajnr.A2890

mean interval between symptom occurrence and DECT scanning was 4.3 days (range, 3 hours to 17 days).

CT Technique

We used the same 64-channel multidetector dual-source CT equipment (Somatom Definition; Siemens, Forchheim, Germany) for all patients. Precontrast (TNC) scans were obtained in single-energy mode, and postcontrast scans in, dual-energy mode. Postcontrast CT scans were obtained during arterial and venous phases, with large arteries assessed on arterial phase CT angiography, and mass lesions and the venous system, on venous phase CT. TNC CT was performed at 120 kV and 100 mAs; with collimation, section thickness, and increments of 0.6, 1.0, and 0.5 mm, respectively; and a pitch of 0.8. For postcontrast scans, 2 different tube voltages and currents were used simultaneously: tube A at 140 kV and 50 mAs and tube B at 80 kV and 200 mAs. For the arterial phase, 60 mL of iodine contrast material was injected at a rate of 4 mL/s, and scanning was started 4 seconds after attenuation in the ascending aorta reached 100 HU. For the venous phase, a second 60-mL aliquot of iodine was injected at 2.5 mL/s immediately after the first injection, followed by 30 mL of saline, and scanning was started 45 seconds after the beginning of the first injection. The other scan parameters were the same as those used in single-energy TNC CT.

Image Postprocessing

TNC images were reconstructed with a 5-mm thickness/interval in the main console and were transferred to the PACS. Postcontrast images were reconstructed with 1-mm thickness/interval and transferred to the workstation (syngo Multimodality; Siemens) for further processing. A diagram of the postprocessing pathway of DECT images is shown in Fig 1. Enhanced average images were produced by mixing 80 kV and 140 kV datasets at a ratio of 3:7; the resulting EA images were equivalent to conventional enhanced CT images obtained at approximately 120 kV. Using dual-energy-analysis material-decomposition software (syngo Dual-Energy Brain Hemorrhage, Siemens), we produced iodine overlay images, VNC images, fusion images of iodine overlay and VNC images from the 2 sets of images (Fig 2). The iodine component detected with the DECT technique was displayed in red in the iodine overlay and fusion images. Principles of the material decomposition mechanism are schematically shown in Fig 3. VNC images were produced at 5-mm thickness and intervals for comparison with TNC images. All other images were obtained as MPRs with 1-mm thickness and intervals in the workstation. Fusion images were produced from venous phase images.

Additional volume-rendering image reconstruction (syngo Dual-Energy, Siemens) was performed by using dual-energy bone removal for CT angiography with/without CT venography for detection of other underlying causes of vascular origin. All the images reconstructed in the workstation were transferred to the PACS for image interpretation and comparison.

Comparisons

Two experienced radiologists (H.K.L., H.Y.L.) with 6 years of experience evaluated the images, with final decisions made by consensus. They were blinded to the clinical history of each patient. Inter-rater agreement was measured by using weighted κ statistics.

Comparison of the Diagnostic Performance of EA and Fusion Images

The diagnostic performance of EA images (equivalent to conventional single-energy postcontrast images) alone, EA images combined with TNC images (equivalent to single-energy pre- and postcontrast images), and fusion images (postcontrast DECT images) was compared for their ability to detect underlying tumors. The presence of tumor was assessed on a 5-point scale based on contrast enhancement in or adjacent to the hematoma: grade 1 = definitely no, representing no enhancement; grade 2 = probably no, representing focal minimal enhancement; grade 3 = equivocal but less likely, representing thin rim or curvilinear enhancement but less likelihood of tumor; grade 4 = probably yes, representing a thick rim or irregular enhancement; and grade 5 = definitely yes, representing definite mass enhancement. An ROC curve was constructed for each image set, and the AUC for each set was compared. The sensitivity, specificity, positive predictive value, and negative predictive value of each image set were calculated with grades 4 and 5 regarded as positive for tumor presence.

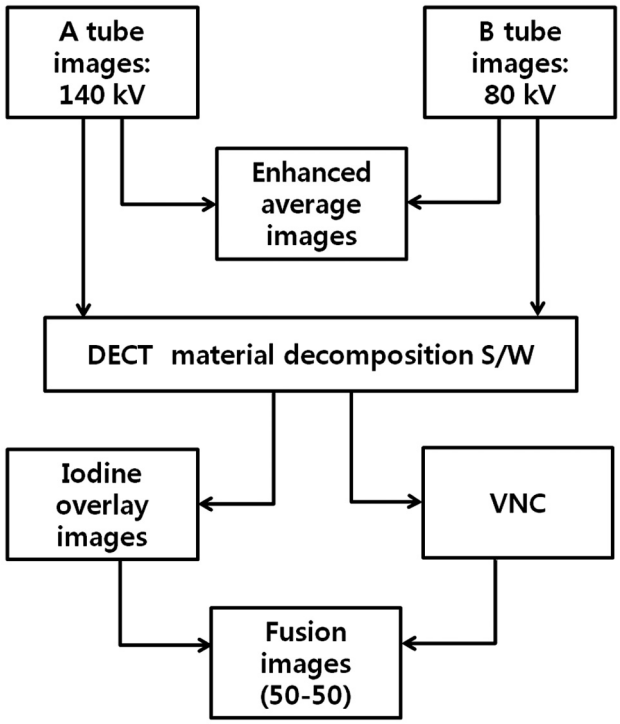

Fig 1. Diagram of image postprocessing of DECT for analysis of hematoma. Enhanced average images, which are equivalent to conventional enhanced images, are produced by mixing and averaging the CT numbers of corresponding voxels at a 7:3 ratio of A and B tube images. Using dual-energy material decomposition software, we separated the iodine component from the images obtained from the A and B tubes; this iodine component is shown in iodine-overlay images and displayed in red. Virtual noncontrast images are generated by removing iodine from the source images. Fusion images are obtained by mixing iodine overlay images and virtual noncontrast images, typically at a ratio of 50:50.

Comparison of TNC and VNC Images

The image noise and overall image quality of TNC and VNC images in evaluating hematomas were compared subjectively. Noise level was assessed by using a 3-point scale: 1, TNC noise > VNC noise; 2, TNC noise = VNC noise; and 3, VNC noise > TNC noise. Overall image quality was assessed by using a similar 3-point scale: 1, VNC > TNC; 2, VNC = TNC; and 3, TNC > VNC. Images were compared objectively by assessing CNR of the hematomas. Each CNR was calculated by dividing the difference in the CT number of each hematoma and normal-looking white matter by the SD of the CT number of CSF in the ventricle. The CT number was measured in the hematoma, white matter, and lateral ventricle. Three ROIs were delineated in each, and

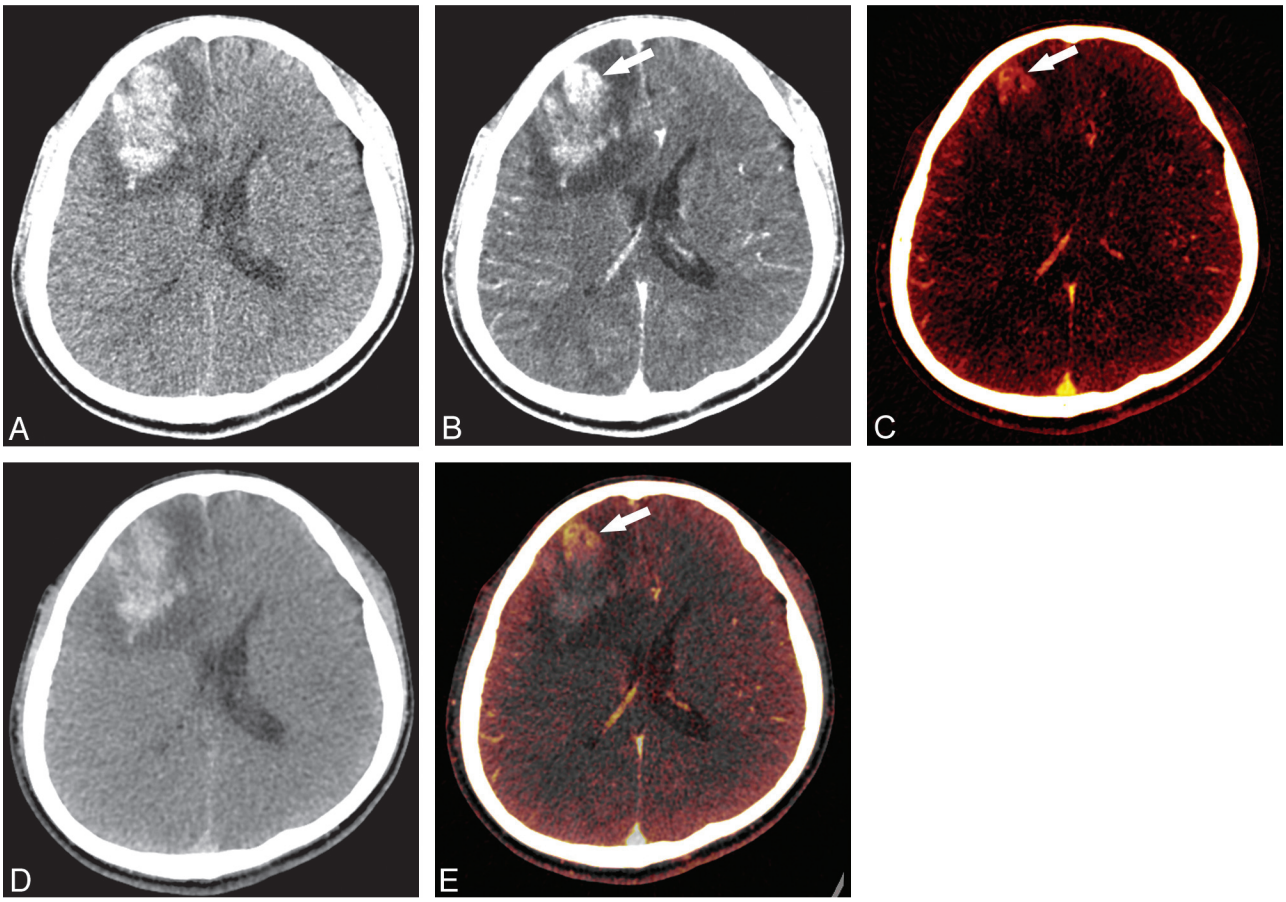

Fig 2. A 35-year-old man with known renal cell carcinoma and pulmonary metastasis. *A*, True noncontrast CT shows hemorrhage in the right frontal lobe. *B*, Enhanced average image obtained by mixing 80- and 140-kV images. A small area of enhancement is suspected in the anterior portion of the hematoma (*arrow*). Iodine overlay image (*C*) and virtual noncontrast image (*D*) obtained by postprocessing of 80- and 140-kV images by using dual-energy material decomposition software. The iodine component is displayed in red in the iodine-overlay image, and the enhancing tumor portion is clearly identified (*arrow*). High attenuation of hemorrhage is not visualized in this image set, but high attenuation of the bony structure is preserved (*C*). Virtual noncontrast image (*D*) shows the hematoma clearly, but the image is smoothed compared with the true noncontrast image in *A*. *E*, Fusion image obtained by mixing of iodine-overlay and virtual noncontrast images clearly shows an enhancing mass in the anterior portion of the hematoma (*arrow*). The brain lesion was histologically confirmed as a hemorrhagic metastasis from renal cell carcinoma.

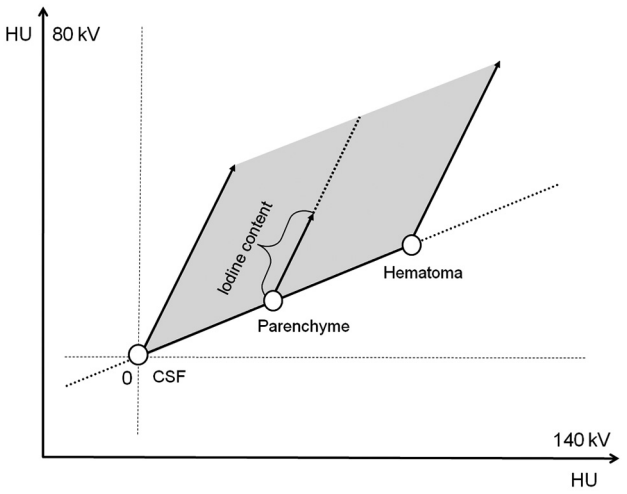

Fig 3. Mechanism of differentiating hematoma and iodine. Measured voxel values are plotted on the 2-energy scatterplot. CSF, brain parenchyma, and hematoma have similar CT numbers on both 80- and 140-kV images. In contrast, iodine has nearly a 2 times higher CT number on 80 kV images compared with 140 kV. Therefore, voxels in the area of gray shading represent various amounts of iodine content.

the mean values of the ROIs were used. The McNemar test and Student *t* test were used for comparisons.

Table 1: Underlying pathology of ICH

Underlying Pathology	Patient No.
Tumor	17
Metastases, including melanomas	13 (4 melanomas)
Primary (astrocytoma[a]/PNET/meningioma)	4 (1/1/2)
Nontumor	39
Unrecognized hypertensive	9
Infarct, HT/coagulopathy/trauma	2/8/4
AVM/DAVF/CM	3/1/3
Amyloid angiopathy/Moyamoya disease/vasculitis	1/1/2
Dural sinus thrombosis/occlusion	5
Total	56

Note:—PNET indicates primitive neuroectodermal tumor; infarct, HT, infarct, hemorrhagic transformation; DAVF, dural arteriovenous fistula; CM, cavernous malformation.
[a] Gemistocytic astrocytoma grade II.

A P value $< .05$ was considered significant. Statistical analysis was performed by using the Statistical Package for the Social Sciences for Windows (Version 18.0; SPSS, Chicago, Illinois) or MedCalc for Windows (Version 10; MedCalc Software, Mariakerke, Belgium).

Results

Of the 56 included patients, 17 had primary or metastatic tumors and 39 had nontumorous ICH (Table 1). Of the 17 patients with tumors, 13 had metastatic tumors and 4 had pri-

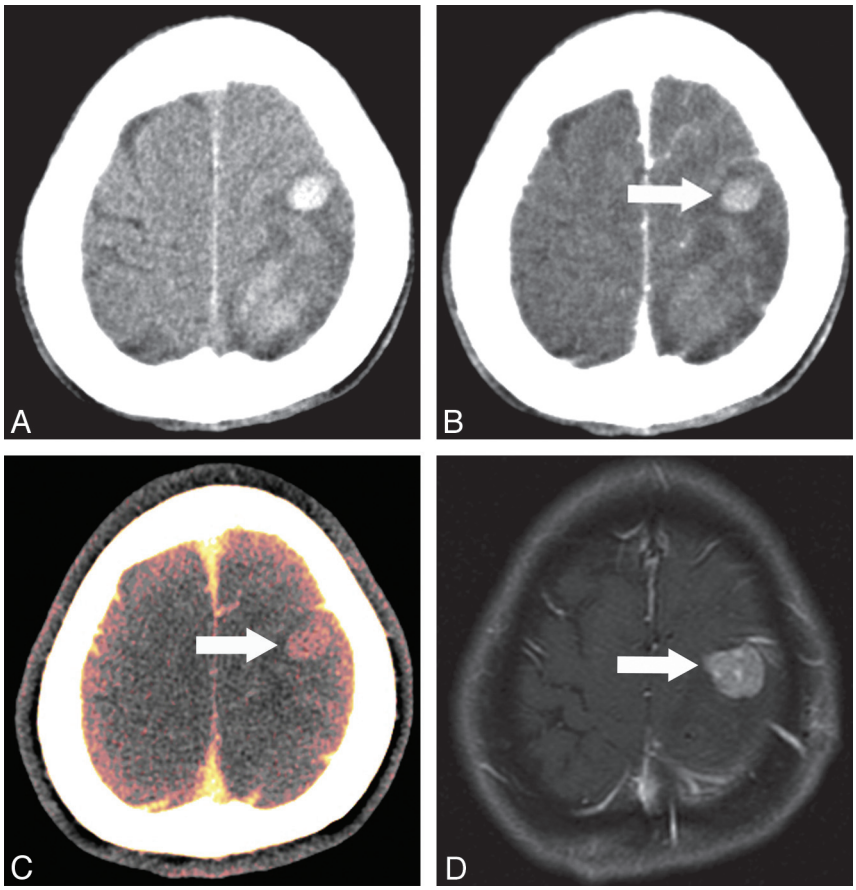

Fig 4. A 37-year-old woman with known hepatocellular carcinoma. *A,* True noncontrast CT image shows acute ICH in the left frontal lobe. Part of a separate lesion is noted in the left parietal lobe. *B,* Enhanced average image at the corresponding level fails to show enhancement in the frontal lobe lesion (*arrow*). The parietal lobe lesion showed irregular rim enhancement in the main body of the hematoma (not shown here). *C,* DECT fusion image clearly shows the frontal lobe lesion in red, representing the iodine component (*arrow*). *D,* The parietal lobe lesion was surgically removed and confirmed as a metastasis, but the frontal lobe lesion was not treated initially. Gadolinium-enhanced MR imaging performed 1 month later clearly shows the lesion in the left frontal lobe; its size has increased (*arrow*).

mary tumors. Because 1 patient with metastatic tumors had 2 separate but closely located hemorrhagic metastatic lesions (Fig 4), the total number of tumor ICH lesions was 18. Of these 17 patients with tumor bleeding, 12, including all 4 patients with primary tumors, were diagnosed pathologically, whereas 5 of 13 metastatic tumors were diagnosed on the basis of clinical background and additional or follow-up imaging, including MR imaging. The 39 patients with nontumorous ICH included unrecognized hypertensive ICH, unrecognized traumatic ICH, coagulopathies of various origins, hemorrhagic transformation of acute infarction, and various kinds of vascular-origin diseases (Table 1). Of these 39 patients, 5, including 3 cases of cavernous malformations and 2 cases of AVMs, were diagnosed on the basis of surgical results. All vascular lesions, including AVMs, dural arteriovenous fistula, Moyamoya disease, and vasculitis, were diagnosed by conventional angiography. Dural sinus thromboses or occlusion was diagnosed by conventional angiography and/or CT venography. Hemorrhagic transformation of infarction or initially unrecognized trauma was diagnosed by accompanying imaging findings and resolution of the lesion on imaging follow-up. One case of amyloid angiopathy was diagnosed by MR gradient-echo images. Diagnosis of unrecognized hypertensive ICH or ICH due to coagulopathy was based on the clinical information and resolution of lesions on follow-up. Patients in whom underlying causes were unproven were excluded in the analysis.

Of the 18 tumorous lesions, 17 were correctly diagnosed on fusion images, 12 on combined EA and TNC images, and 11 on EA images alone. All CT imaging sequences missed 1 case of ICH from a hepatoma metastasis (Fig 5). MR imaging performed on the same day also failed to detect a tumor in that case. Follow-up MR imaging performed 1 month later revealed a metastatic mass in the hematoma area with other multiple metastatic foci; therefore, this case was considered a false-negative. A cavernous malformation was the only false-positive diagnosis on fusion images (Fig 6); it was diagnosed as a tumor by all CT imaging sequences but surgery revealed a cavernous malformation.

The diagnostic performance of fusion images was higher than that of either EA images alone or combined EA and TNC images in detecting brain tumors; the sensitivities of these 3 methods were 94.4%, 61.1%, and 66.7%, respectively; and their specificities were 97.4%, 92.3%, and 89.7%, respectively (Table 2). The AUCs of the ROC curves were 0.964, 0.786, and 0.842, respectively (Fig 7). There were significant differences between fusion and EA images ($P = .006$) and between fusion and combined EA and TNC images ($P = .011$), but not between EA and combined EA and TNC images ($P = .353$).

On visual assessment, image noise was similar between

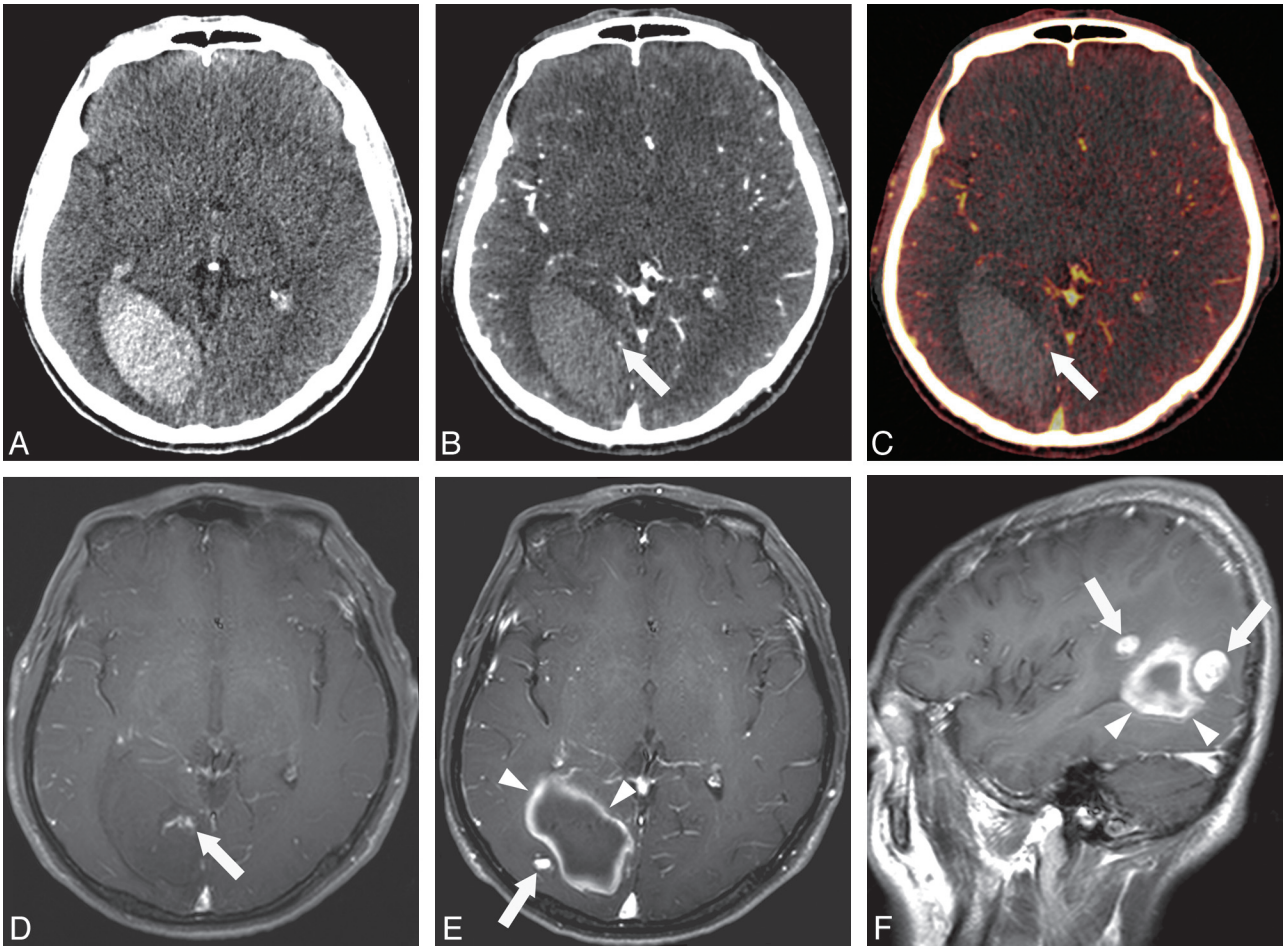

Fig 5. A false-negative result of DECT in a 48-year-old man with known hepatocellular carcinoma. *A*, True noncontrast CT shows a hematoma in the right occipital lobe. Small dotlike enhancement is noted in the medial aspect of hematoma on an enhanced average image (*B*) and a fusion image (*C*). However, no definite mass lesion is identified. *D*, On the enhanced T1-weighted image, some tubular enhancement is noted (*arrow*), but a tumorous lesion is not definite. *E* and *F*, One-month follow-up axial and sagittal postcontrast MR images show multiple enhancing nodules (*arrows*) around the hematoma (*arrowheads*). These strongly suggest the possibility of previous ICH caused by underlying metastatic tumor.

VNC and TNC images (McNemar test, $P = .089$). However, on the objective assessment by measurement of the SD of the CT number in the lateral ventricle, the noise is lower with VNC compared with TNC images (Table 3). The overall image quality of TNC images was better than that of VNC images ($P < .001$). The CT number of hematomas was higher on TNC than on VNC images. The CT number for white matter was not significantly different between VNC and TNC images. The CNR was higher on VNC than on TNC images (paired *t* test, $P < .01$) (Table 3).

Interobserver agreement was substantial to almost perfect between the 2 readers in all comparison studies performed in our series (range of weighted κ value from 0.617 to 0.928).

Discussion

In this study, we intended to investigate the utility of DECT for detecting underlying tumors in case of acute ICH compared with the conventional CT. We found that DECT fusion images were more sensitive than either EA images (equivalent to conventional postcontrast CT) alone or combined EA and TNC images in detecting underlying tumors, a result confirmed by ROC curve analysis. In addition, the higher negative predictive value of fusion images compared with EA images indicates that the absence of underlying tumors in a patient with ICH can be stated more confidently. The higher sensitivity of DECT fusion images is attributable to the ability of DECT to separate iodine from hematoma. The iodine component was displayed in red and was readily distinguished from hematoma. On EA images, densely enhancing tumors with sufficient size were not difficult to detect. However, it was difficult to differentiate high-attenuation hematoma and tumor enhancement on EA images when tumor enhancement was not sufficiently attenuated or when the enhancing tumor portion was small.

DECT can be used to differentiate the high attenuation of hematomas and that of iodine because the x-ray attenuation as a function of photon energy is different for the 2 materials.[19] In the energy range used for CT, x-ray attenuation is mainly due to photoelectric effect and Compton scattering. While the photoelectric effect is strongly energy-dependent, Compton scattering is not. As a consequence, CT attenuation depends on the photon energy and the atomic number and concentration of the material being scanned. Thus, materials can be differentiated by using different x-ray spectra, an effect that is particularly useful for materials of a large atomic number due to the photoelectric effect.[20] Iodine has a high atomic number

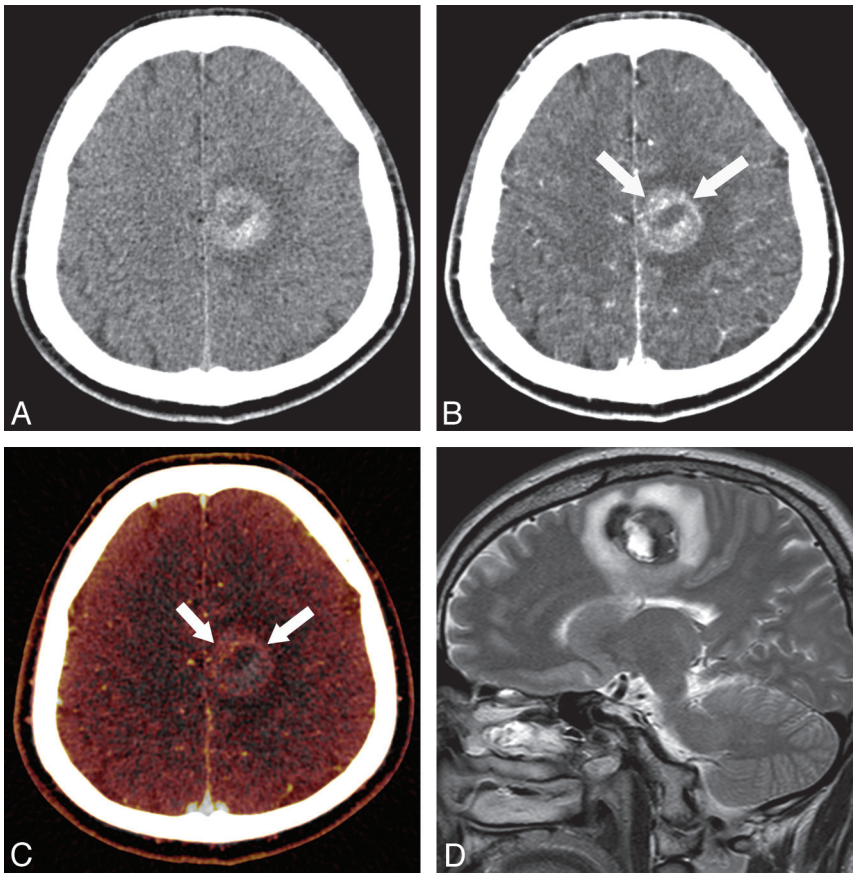

Fig 6. A false-positive result of DECT in a 50-year-old man with right-sided weakness commencing 3 days earlier. *A*, True noncontrast CT shows a hematoma in the left frontal lobe superior frontal gyrus. A thin irregular rim-enhancing lesion is shown on the enhanced average image (*B*) and fusion image (*C*) (*arrows*). *D*, T2-weighted sagittal image shows a multilocular dark-signal-intensity lesion mixed with high signal intensity with a dark-signal-intensity rim, suggesting multiple-stage hemorrhage. On the basis of images *B* and *C*, a hemorrhagic tumor was suspected, but the diagnosis was changed after reviewing MR imaging, which suggested the possibility of a cavernous malformation. Diagnosis of a cavernous malformation was confirmed by surgery.

Table 2: Sensitivity, specificity, PPV, and NPV of each image series

	Sensitivity (%) (CI)	Specificity (%) (CI)	PPV (%) (CI)	NPV (%)(CI)
Fusion images	94.4 (72.6–99.1)	97.4 (86.5–99.6)	94.4 (72.6–99.1)	97.4 (86.5–99.6)
EA images	61.1 (35.8–82.6)	92.3 (79.1–98.3)	78.6 (49.2–95.1)	83.7 (69.3–3.2)
EA + TNC images	66.7 (41.0–6.6)	89.7 (75.8–97.1)	75.0 (47.6–92.6)	85.4 (70.8–94.4)

Note:—CI indicates confidence interval; PPV, positive predictive value; NPV, negative predictive value.

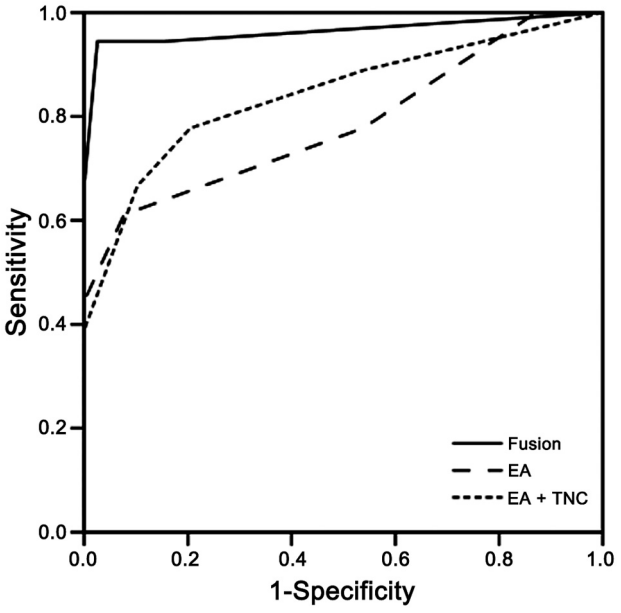

Fig 7. ROC curves for fusion, EA, and EA + TNC images. Fusion images show the highest performance with an AUC of 0.964.

and shows a high attenuation difference between high- and low-energy x-rays, whereas hematomas do not. The CT number of a typical acute ICH approaches approximately 80 HU, and the differences at 80 and 140 kV are not significant; in contrast, the CT number of iodine at 80 kV is approximately twice that at 140 kV.[21] This is the basic mechanism used for differentiating iodine from acute ICH (Fig 3).

We compared the noise level and overall image quality of VNC and TNC images. We found that image noise was equal between VNC and TNC images and the overall image quality of VNC was lower than that of TNC images. Although image noise between VNC and TNC images was similar on visual inspection, the noise level measured in CSF was significantly lower with VNC compared with TNC images. The lower noise level and lower image quality for VNC were also reported in previous studies, and this may be related to pre- and postpro-

Table 3: Comparison of CT numbers of ICH and white matter, SD of CSF, and CNR on TNC and VNC images (mean ± SD)[a]

	TNC Images	VNC Images	*P* Value
ICH	71.5 ± 7.3	62.8 ± 9.6	.000
White matter	31.0 ± 2.0	31.2 ± 3.0	.675
SD of CSF	6.1 ± 1.5	3.7 ± 0.6	.000
CNR	7.0 ± 1.9	8.8 ± 3.0	.000

[a] Values are HU in ICH, white matter, SD of CSF, and ratio in CNR.

cessing methods as well as the tube energy used.[22-24] Although VNC images had some limitations compared with TNC images, such as lower image quality and lower CT number of hematomas, VNC could detect ICH in all patients. Thus, VNC images may replace TNC images. Our results are in good agreement with those of previous studies, which showed that though the quality of VNC images was not better than that of TNC images, VNC images were clinically feasible and useful in examinations of the abdomen and brain.[23,25,26]

DECT with CT angiography and fusion images seems to be an ideal tool in evaluating patients with ICH in the acute stage. By obtaining CT angiography source images in dual-energy mode, both bone-removed CT angiography for vessel evaluation and fusion images for tumor evaluation can be produced from the same source data. Both arterial and venous phase DECT scans are necessary for the ideal assessment of unknown-origin ICH. Although arterial phase CT angiography can reveal various vascular lesions, it is not sufficient for obtaining optimal tumor enhancement. Venous phase CT can provide better tumor enhancement. At the same time, CT venography obtained from venous phase CT can be used for screening dural sinus thrombosis, a condition that is sometimes difficult to diagnose. DECT fusion images can be obtained from both arterial and venous phase image sets. Our early experience suggested that though both sets are equally capable of detecting lesions, lesion conspicuity was better with venous phase images.

Although MR imaging is known to be better than CT for the detection of underlying tumor in case of tumor bleeding, sometimes underlying tumors may be masked in the acute or subacute stage, and it is often necessary to perform follow-up MR imaging.[13,16,17] In contrast, DECT can allow detection of tumor in the acute stage of bleeding, and this may enable detection of tumor at the time of patient presentation and may obviate follow-up MR imaging for screening of tumor. DECT can also allow preclusion of the existence of tumor in acute-stage ICH. These are important advantages of DECT for the proper management of patients. In addition, vessels can be evaluated with the same source data. In that sense, DECT can be used as a screening tool in cases with uncertain-origin ICH. However, we did not compare the diagnostic performance directly between DECT fusion images and MR imaging because MR imaging was obtained in a limited number of our patients.

The radiation dose of a single set of DECT is approximately 1 mSv, similar to that of an enhanced scan of conventional CT angiography.[18,25] The radiation dose of typical conventional CT angiography, including precontrast images, is 1.9 mSv.[27] The average radiation dose per patient in our series was about 2.9 mSv. The radiation dose in our series was higher than that of conventional CT angiography because we obtained 3 sequences, including a TNC scan and 2 phases of DECT (ie, arterial and venous phases). Our results suggest that the radiation dose in DECT can be reduced by replacing TNC CT with VNC images in patients with known ICH. As a next step, the radiation dose can be potentially reduced further by omitting 1 of the 2 phases of DECT scanning through optimizing the time sequence. DECT with CT angiography may be needed only 1 time during the patient's clinical course and may potentially reduce the radiation dose indirectly by obviating other screening studies.

Our study had several limitations. The first is a relatively high proportion of tumor bleeding compared with other studies. The main reason is that we excluded patients with obvious hypertension and ICH. However, there may have been some patient-selection bias because DECT was performed as a referral base for patients with ICH of uncertain etiology at our institution and those referred from other hospitals. By the same token, as the second limitation, DECT was not the initial imaging technique, and this explains the rather widespread lapse in time from symptom onset to DECT scanning in our patients. However, we excluded patients without high attenuation at the time of examination or data review, and all included patients had variable degrees of high attenuation. This was not likely to have influenced our evaluation of the diagnostic performance of DECT. The third limitation is lack of pathologic backup in 5 of 13 metastatic tumors. However, either primary or metastatic tumors at other body sites were proved pathologically in all cases, and unequivocal enhancing lesions were visualized in the brain on postcontrast CT or MR imaging; therefore, invasive surgery was not indicated in those patients.

Conclusions

We investigated the clinical utility of DECT in the differentiation of tumor bleeding from pure ICH. DECT fusion images produced from iodine overlay and VNC showed higher sensitivity and specificity than EA images (equivalent to conventional postcontrast CT) in detecting underlying tumors in patients with acute ICH. DECT is a useful tool in differentiating tumor bleeding and pure ICH in patients with acute ICH of unclear origin.

Disclosures: Bernhard Krauss—*UNRELATED: Employment*: Siemens AG.

References

1. Broderick JP, Brott T, Tomsick T, et al. **The risk of subarachnoid and intracerebral hemorrhages in blacks as compared with whites.** *N Engl J Med* 1992;326:733–36
2. Furlan AJ, Whisnant JP, Elveback LR. **The decreasing incidence of primary intracerebral hemorrhage: a population study.** *Ann Neurol* 1979;5:367–73
3. Qureshi AI, Tuhrim S, Broderick JP, et al. **Spontaneous intracerebral hemorrhage.** *N Engl J Med* 2001;344:1450–60
4. Fewel ME, Thompson BG, Hoff JT. **Spontaneous intracerebral hemorrhage: a review.** *Neurosurg Focus* 2003;15:E1
5. Destian S, Sze G, Krol G, et al. **MR imaging of hemorrhagic intracranial neoplasms.** *AJR Am J Roentgenol* 1989;152:137–44
6. Barkovich AJ, Atlas SW. **Magnetic resonance imaging of intracranial hemorrhage.** *Radiol Clin North Am* 1988;26:801–20
7. Delgado Almandoz JE, Romero JM, Pomerantz SR, et al. **Computed tomography angiography of the carotid and cerebral circulation.** *Radiol Clin North Am* 2010;48:265–81
8. Delgado Almandoz JE, Schaefer PW, Forero NP, et al. **Diagnostic accuracy and yield of multidetector CT angiography in the evaluation of spontaneous in-**

traparenchymal cerebral hemorrhage. *AJNR Am J Neuroradiol* 2009; 30:1213–21
9. Romero JM, Artunduaga M, Forero NP, et al. **Accuracy of CT angiography for the diagnosis of vascular abnormalities causing intraparenchymal hemorrhage in young patients.** *Emerg Radiol* 2009;16:195–201
10. Yeung R, Ahmad T, Aviv RI, et al. **Comparison of CTA to DSA in determining the etiology of spontaneous ICH.** *Can J Neurol Sci* 2009;36:176–80
11. Yoon DY, Chang SK, Choi CS, et al. **Multidetector row CT angiography in spontaneous lobar intracerebral hemorrhage: a prospective comparison with conventional angiography.** *AJNR Am J Neuroradiol* 2009;30:962–67
12. Scott M. **Spontaneous intracerebral hematoma caused by cerebral neoplasms: report of eight verified cases.** *J Neurosurg* 1975;42:338–42
13. Licata B, Turazzi S. **Bleeding cerebral neoplasms with symptomatic hematoma.** *J Neurosurg Sci* 2003;47:201–10, discussion 210
14. Schrader B, Barth H, Lang EW, et al. **Spontaneous intracranial haematomas caused by neoplasms.** *Acta Neurochir (Wien)* 2000;142:979–85
15. Inamasu J, Kuramae T, Nakatsukasa M. **Glioblastoma masquerading as a hypertensive putaminal hemorrhage: a diagnostic pitfall.** *Neurol Med Chir (Tokyo)* 2009;49:427–29
16. Atlas SW, Grossman RI, Gomori JM, et al. **Hemorrhagic intracranial malignant neoplasms: spin-echo MR imaging.** *Radiology* 1987;164:71–77
17. Meyer JR, Gorey MT. **Differential diagnosis of nontraumatic intracranial hemorrhage.** *Neuroimaging Clin N Am* 1998;8:263–93
18. Deng K, Liu C, Ma R, et al. **Clinical evaluation of dual-energy bone removal in CT angiography of the head and neck: comparison with conventional bone-subtraction CT angiography.** *Clin Radiol* 2009;64:534–41
19. Gupta R, Phan CM, Leidecker C, et al. **Evaluation of dual-energy CT for differentiating intracerebral hemorrhage from iodinated contrast material staining.** *Radiology* 2010;257:205–11
20. Johnson TR, Krauss B, Sedlmair M, et al. **Material differentiation by dual energy CT: initial experience.** *Eur Radiol* 2007;17:1510–17
21. Behrendt FF, Schmidt B, Plumhans C, et al. **Image fusion in dual energy computed tomography: effect on contrast enhancement, signal-to-noise ratio and image quality in computed tomography angiography.** *Invest Radiol* 2009; 44:1–6
22. Mahgerefteh S, Blachar A, Fraifeld S, et al. **Dual-energy derived virtual nonenhanced computed tomography imaging: current status and applications.** *Semin Ultrasound CT MR* 2010;31:321–27
23. Graser A, Johnson TR, Hecht EM, et al. **Dual-energy CT in patients suspected of having renal masses: can virtual nonenhanced images replace true nonenhanced images?** *Radiology* 2009;252:433–40
24. Yu L, Primak AN, Liu X, et al. **Image quality optimization and evaluation of linearly mixed images in dual-source, dual-energy CT.** *Med Phys* 2009; 36:1019–24
25. Thomas C, Ketelsen D, Tsiflikas I, et al. **Dual-energy computed tomography: is there a penalty in image quality and radiation dose compared with single-energy computed tomography?** *J Comput Assist Tomogr* 2010;34:309–15
26. Ferda J, Novak M, Mirka H, et al. **The assessment of intracranial bleeding with virtual unenhanced imaging by means of dual-energy CT angiography.** *Eur Radiol* 2009;19:2518–22
27. Cohnen M, Wittsack HJ, Assadi S, et al. **Radiation exposure of patients in comprehensive computed tomography of the head in acute stroke.** *AJNR Am J Neuroradiol* 2006;27:1741–45